Research Article

Jili Lu, Qingyun Yang, Zhongliang Meng, Kang Yang, Wei Xu and Ching Vincent Chiu*

Modeling and dynamic analysis of functionally graded porous spherical shell based on Chebyshev–Ritz approach

https://doi.org/10.1515/secm-2022-0214
received December 20, 2022; accepted June 07, 2023

Abstract: This study proposes a unified modeling method to investigate the dynamic behaviors of the functionally graded porous (FGP) spherical shell with elastic boundary conditions. First, three kinds of FGP distributed patterns are defined. Then, the first-order shear deformation theory is selected to build the governing equations of the spherical shell with elastic boundary conditions, which can be solved by the Rayleigh–Ritz approach. Moreover, Chebyshev polynomials of the third kind are selected as an admissible function to express the motion equation. With the constructed model, the correctness is verified by comparing the natural frequency and forced response obtained from both open literature and finite element method. Ultimately, the parameter study is conducted to conclude the effect of the design parameter on the dynamic characteristics of the spherical shell.

Keywords: dynamic analysis, functionally graded porous material, spherical shell, elastic boundary conditions

Nomenclature

notation	definition
A_{ij}	stretching stiffness
B_{ij}	stretching-bending coupling stiffness
D_{ij}	bending stiffness
e_0	porosity coefficient
e_m	mass density coefficient
$E(z)$	Young's modulus
E_1	maximum values of Young's modulus
E_2	minimum values of Young's modulus
$G(z)$	shear modulus
G_1	maximum values of shear modulus
G_2	minimum values of shear modulus
q_0	amplitude of loading pulse
t	time
u	displacement of meridional direction
$U_m/V_m/W_m/\psi_{\varphi m}/\psi_{\theta m}$	the unknown coefficients of different displacement functions
v	displacement of circumferential direction
w	displacement of normal direction
z	normal direction
$\rho(z)$	mass density of FGP material
ρ_1	maximum values of mass density
ρ_2	minimum values of mass density
ψ_φ	rotations relative to φ coordinate
ψ_θ	rotations relative to θ coordinate
$\varepsilon^0_{\varphi\varphi}/\varepsilon^0_{\theta\theta}/\varepsilon^0_{\varphi\theta}$	strains of surface
$\kappa_{\varphi\varphi}/\kappa_{\theta\theta}/\kappa_{\varphi\theta}$	curvatures
θ	circumferential direction
φ	meridional direction
φ_0	top boundary of spherical shell
φ_1	bottom boundary of spherical shell

1 Introduction

Spherical shell is a kind of fundamental structure with high stiffness and light weight, which has been widely used in many fields such as architecture, turbine, and launch vehicle. In practical applications, spherical shell may produce vibration, structural fatigue, and noise because of the excitations of the external environment [1]. These undesirable effects can be suppressed and reduced by constructing a spherical shell with excellent vibration characteristics.

To improve the vibration characteristics of spherical shells, many studies have been carried out [2–4]. In the

* **Corresponding author: Ching Vincent Chiu,** College of Mechanical & Electrical Engineering, Zaozhuang University, Zaozhuang, China, e-mail: cvinchiu@163.com
Jili Lu, **Qingyun Yang**, **Kang Yang**, **Wei Xu:** College of Mechanical & Electrical Engineering, Zaozhuang University, Zaozhuang, China
Zhongliang Meng: School of Mechanical Engineering, Shandong University, Shandong, China

study by Adin and Adin [5], mechanical properties of composite materials produced from woven jute type were investigated. In the study by Song and Ge [6], a joined composite shell was presented, and its dynamic response was explored.

In the study by Adin and Kılıçkap [7], considering the effects of high satiety, fracture strength, and good dimensional stability, glass fiber-reinforced composite materials have widespread uses. In the study by Hamit et al. [8], considering the effect of materials, the fatigue behavior of composite patched and non-patched aluminum plates was numerically investigated. The study revealed that the composite patch's contribution is very important. In the study by Panda and Singh [9], laminated composite was introduced into a spherical shell, and its nonlinear free vibration was studied. In the study by Mahapatra and Panda [10], a laminated composite spherical shell under hygrothermal loading was presented, and its nonlinear free vibration was investigated. The fiber-reinforced composite materials possess higher strength and modules than general laminated composite materials. Hence, a fiber-reinforced spherical shell was prepared by Ram and Babu [11], and its free vibration was studied. Besides, functionally graded (FG) material is also of interest to some researchers. In the study by Su et al. [12], the vibration behavior of the FG spherical shell with arbitrary boundary conditions was investigated. In the study by Duc et al. [13], the nonlinear dynamic behaviors of the FG spherical shell were investigated, and the effect of elastic foundations and temperature was studied. Due to the significant practical application of such structures, some researchers studied their mechanical behaviors via different approaches. In the study by Duc et al. [13], the vibrational behavior of FG spherical shells resting on an elastic substrate was studied. In the study by Xie et al. [14], the effects of elastic boundary conditions on the free vibration behavior of thin spherical shells have been examined. In the study by Duc et al. [13], nonlinear dynamic behaviors of annular spherical shells made of nano-composite materials have been studied. In the study by Li et al. [15], the authors provided a semi-analytical approach for examining the linear vibration behavior of annular spherical shells under different edge conditions. Nevertheless, the aforementioned studies only focus on the improvement of the stiffness and neglected design for light weight, which results in higher weight. Within the framework of the thin-walled shell theory, Li et al. [16,17] investigated the buckling behaviors of confined functionally graded porous (FGP) rectangular arches reinforced with graphene platelets and subjected to a concentrated load and uniform pressure. Their results show that the critical buckling load of porous arches is considerably affected by the porous coefficient and graphene platelets (GPL) weight fraction. Li [18] subsequently extended this work to the partially confined FGP–GPL reinforced composite arches and suggested that a greater contact area with the medium gives a higher buckling load. Liu et al. [19] presented a buckling analysis of FGP circular shallow arches based on the Euler–Bernoulli hypothesis and found that the FGP arches have a good performance in weight reduction and a high strength-to-weight ratio. Therefore, the study of the FGP spherical shell is significant to the development of technology and engineering application. However, there are few discussions about the FGP spherical shell and its vibration characteristics. In this context, the vibration characteristics of the FGP spherical shell are studied in this work.

To better understand the vibration characteristics of the FGP structures, the primary task is to investigate its free vibration by utilizing appropriate methods [20–24]. There were some relative works about FGP plates recently. The higher order shear deformationtheories combined with the finite element method were used to investigate FGP plate vibrations [25]. The vibration study on the FGP structure elements of revolution with general elastic boundary conditions was published [26]. Duc et al. [27] analyzed the nonlinear buckling and post-buckling characteristics of conical sandwich shells with FGP sandwich materials. Van et al. [28] published an article on the free and forced vibration study about truncated conical FGP panel using analytical method. Duc et al. [29] studied the nonlinear dynamic vibration of FGP shells with elastic foundation based on first-order shear deformation theory (FSDT) in the same year. The free vibration of the FGP beam was studied by utilizing a modified Fourier series method [30]. The free vibration of the FGP rotary structure was examined by combining the FSDT and the Rayleigh–Ritz method [31]. The vibration behavior of FGP micro shells with classical boundary conditions was explored by Salehipour et al. [32]. The limitation of opening studies is increasingly apparent. In engineering applications, forced vibration is the main form of structural vibration. However, most of the current research on FGP spherical shell focus on free vibration and lack of attention to forced vibration. To provide a reference for engineering applications, not only the free vibration, but also the forced vibration of the FGP spherical shell should be further studied.

Previous literature shows that structural vibration behaviors are significantly affected by boundary conditions [33]. A Jacobi–Ritz approach was presented to investigate the effect of arbitrary boundary conditions on the dynamic behaviors of the FGP beam by Qin et al. [34]. Considering the effect of the clamped free boundary, the

first three out-of-plane bending free vibration of symmetric laminated beams is studied by Timoshenko's FSDT by Cünedioğlu and Beylergil et al. [23]. Free vibration responses of damaged beams are examined using Euler–-Bernoulli beam and classical lamination theories [24]. Considering the effect of general boundary condition, the vibration behavior of the FGP cylindrical shell was investigated by Li et al. [35]. The buckling behavior of FG nanoplates with three kinds of arbitrary restraint was studied by Karami et al. [36]. For various work environments, the boundary conditions are different. To satisfy the application requirements, the effect of boundary conditions on the vibration behaviors of the FGP spherical shell should be considered.

The contribution of this study can be summarized as follows: (1) the FGP is introduced in the spherical shell to enhance its dynamic performance and decrease its structural weight; (2) a dynamic model of the FGP spherical shell based on FSDT and three types of Chebyshev polynomials is proposed to improve the modeling precision of the FGP spherical shell; (3) various boundary conditions and porosity distributions are systematically considered in the dynamic characteristics of the FGP spherical shell to explore the effect of the environment and materials. Similar to the aforementioned analysis, this work mainly investigates the vibration behaviors of the FGP spherical shell. The framework of subsequent work is shown as follows: First, the mathematical model of dynamic analysis of spherical shells is established and solved. Next, the numerical result is discussed. Finally, the conclusion of this work is given.

2 Theoretical formulation

2.1 FGP spherical shell

Figure 1 shows the FGP spherical shell model with elastic boundary conditions. $R_\varphi = R\ \sin(\varphi_0 + \varphi)$ indicates the distance from the central axis to each point. The essential properties of FGP material are defined as follows:

$$E(z) = E_1\Theta_i(z), \tag{1a}$$

$$G(z) = G_1\Theta_i(z), \tag{1b}$$

$$\rho(z) = \rho_1\Xi_i(z), \tag{1c}$$

where $\Theta_i(z)$ and $\Xi_i(z)$ $(i = 1, 2, 3)$ denote the three kinds of porosity distributions along the z coordinate, and they can be further expanded as follows:

$$\Theta(z) = \begin{cases} 1 - e_0\cos\left(\dfrac{\pi z}{h}\right) & \text{Type 1} \\ 1 - e_0\cos\left(\dfrac{\pi z}{2h} + \dfrac{\pi}{4}\right) & \text{Type 2} \\ 1 - e_0\alpha & \text{Type 3,} \end{cases} \tag{2a}$$

$$\Xi(z) = \begin{cases} 1 - e_m\cos\left(\dfrac{\pi z}{h}\right) & \text{Type 1} \\ 1 - e_m\cos\left(\dfrac{\pi z}{2h} + \dfrac{\pi}{4}\right) & \text{Type 2} \\ \sqrt{1 - e_0\alpha} & \text{Type 3.} \end{cases} \tag{2b}$$

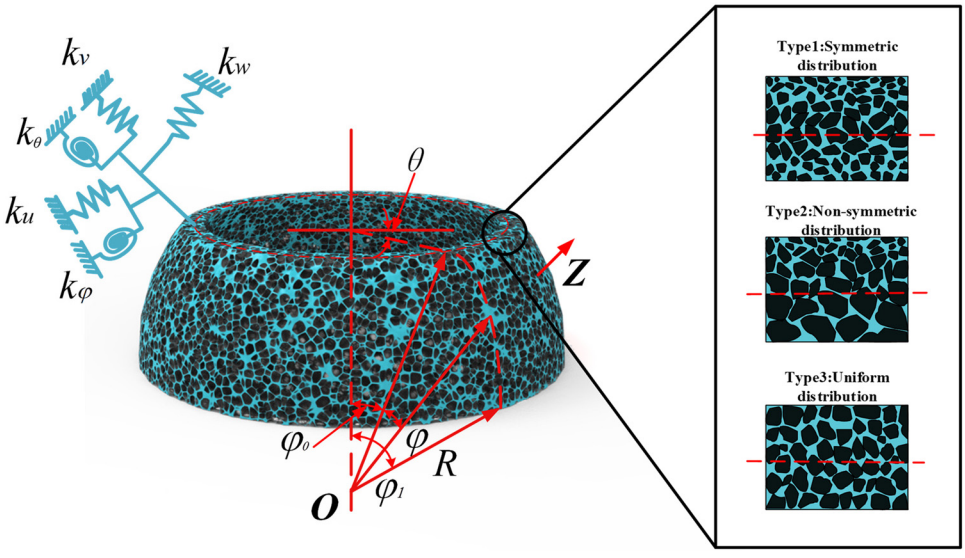

Figure 1: Schematic diagram of FGP spherical shell with elastic boundary conditions.

The functions of e_0 and e_m are defined as follows:

$$e_0 = 1 - \frac{E_2}{E_1} = 1 - \frac{G_2}{G_1} \quad (0 \le e_0 \le 1), \tag{3a}$$

$$e_m = 1 - \frac{\rho_1}{\rho_2} \quad (0 \le e_m \le 1). \tag{3b}$$

The relation equation of e_0 and e_m is given as follows:

$$e_m = 1 - \sqrt{1 - e_0}. \tag{4}$$

2.2 Energy equations

In this study, the displacement components of the FGP spherical shell are derived by utilizing the FSDT as follows:

$$U(\varphi,\ \theta,\ z,\ t) = u(\varphi,\ \theta,\ t) + z\psi_\varphi(\varphi,\ \theta,\ t), \tag{5a}$$

$$V(\varphi,\ \theta,\ z,\ t) = v(\varphi,\ \theta,\ t) + z\psi_\theta(\varphi,\ \theta,\ t), \tag{5b}$$

$$W(\varphi,\ \theta,\ z,\ t) = w(\varphi,\ \theta,\ t). \tag{5c}$$

The normal and shear strains of the FGP spherical shell are obtained by considering the small deformation assumption, and its expressions are given as follows:

$$\varepsilon_{\varphi\varphi} = \varepsilon^0_{\varphi\varphi} + z\kappa_{\varphi\varphi}, \tag{6a}$$

$$\varepsilon_{\theta\theta} = \varepsilon^0_{\theta\theta} + z\kappa_{\theta\theta}, \tag{6b}$$

$$\gamma_{\varphi\theta} = \gamma^0_{\varphi\theta} + z\kappa_{\varphi\theta}, \tag{6c}$$

$$\gamma_{\varphi z} = \psi_\varphi - \frac{u}{R} + \frac{1}{R}\frac{\partial w}{\partial \varphi}, \tag{6d}$$

$$\gamma_{\theta z} = \psi_\theta - \frac{v}{R} + \frac{1}{R_\varphi}\frac{\partial w}{\partial \theta}. \tag{6e}$$

These strains and curvatures can be expanded as follows:

$$\varepsilon^0_{\varphi\varphi} = \frac{1}{R}\frac{\partial u}{\partial \varphi} + \frac{w}{R}, \tag{7a}$$

$$\varepsilon^0_{\theta\theta} = \frac{1}{R_\varphi}\frac{\partial v}{\partial \theta} + \frac{u}{RR_\varphi}\frac{\partial R_\varphi}{\partial \varphi} + \frac{w}{R}, \tag{7b}$$

$$\gamma^0_{\varphi\theta} = \frac{1}{R}\frac{\partial v}{\partial \varphi} - \frac{v}{RR_\varphi}\frac{\partial R_\varphi}{\partial \varphi} + \frac{1}{R_\varphi}\frac{\partial u}{\partial \theta}, \tag{7c}$$

$$\kappa_{\varphi\varphi} = \frac{1}{R}\frac{\partial \psi_\varphi}{\partial \varphi}, \tag{7d}$$

$$\kappa_{\theta\theta} = \frac{1}{R_\varphi}\frac{\partial \psi_\theta}{\partial \varphi} + \frac{\psi_\varphi}{RR_\varphi}\frac{\partial R_\varphi}{\partial \varphi}, \tag{7e}$$

$$\kappa_{\varphi\theta} = \frac{1}{R}\frac{\partial \psi_\theta}{\partial \varphi} - \frac{\psi_\theta}{RR_\varphi}\frac{\partial R_\varphi}{\partial \varphi} + \frac{1}{R_\varphi}\frac{\partial \psi_\varphi}{\partial \theta}. \tag{7f}$$

The relationship between strains and stresses can be defined as follows:

$$\begin{Bmatrix}\sigma_{\varphi\varphi}\\ \sigma_{\theta\theta}\\ \tau_{\varphi\theta}\\ \tau_{\varphi z}\\ \tau_{\theta z}\end{Bmatrix} = \begin{bmatrix}Q_{11} & Q_{12} & 0 & 0 & 0\\ Q_{21} & Q_{22} & 0 & 0 & 0\\ 0 & 0 & Q_{66} & 0 & 0\\ 0 & 0 & 0 & Q_{66} & 0\\ 0 & 0 & 0 & 0 & Q_{66}\end{bmatrix}\begin{Bmatrix}\varepsilon_{\varphi\varphi}\\ \varepsilon_{\theta\theta}\\ \gamma_{\varphi\theta}\\ \gamma_{\varphi z}\\ \gamma_{\theta z}\end{Bmatrix}, \tag{8}$$

where Q_{ij} $(i, j = 1, 2, 6)$ are the stiffness coefficients, which can be further expressed as follows:

$$\begin{aligned} &Q_{11} = Q_{22} = \frac{E(z)}{1 - \nu^2(z)},\ Q_{12} = Q_{21} = \frac{\nu(z)E(z)}{1 - \nu^2(z)},\\ &Q_{66}(z) = \frac{E(z)}{2[1 + \nu(z)]}. \end{aligned} \tag{9}$$

The resulting force and moment of the FGP spherical shell are obtained as follows:

$$\begin{Bmatrix}N_{\varphi\varphi}\\ N_{\theta\theta}\\ N_{\varphi\theta}\\ M_{\varphi\varphi}\\ M_{\theta\theta}\\ M_{\varphi\theta}\end{Bmatrix} = \begin{bmatrix}A_{11} & A_{12} & 0 & B_{11} & B_{12} & 0\\ A_{21} & A_{22} & 0 & B_{21} & B_{22} & 0\\ 0 & 0 & A_{66} & 0 & 0 & B_{66}\\ B_{11} & B_{12} & 0 & D_{11} & D_{12} & 0\\ B_{21} & B_{22} & 0 & D_{21} & D_{22} & 0\\ 0 & 0 & B_{66} & 0 & 0 & D_{66}\end{bmatrix}\begin{Bmatrix}\varepsilon^0_{\varphi\varphi}\\ \varepsilon^0_{\theta\theta}\\ \gamma^0_{\varphi\theta}\\ \kappa_{\varphi\varphi}\\ \kappa_{\theta\theta}\\ \kappa_{\varphi\theta}\end{Bmatrix}, \tag{10a}$$

$$\begin{Bmatrix}Q_{\varphi z}\\ Q_{\theta z}\end{Bmatrix} = \frac{5}{6}\begin{bmatrix}A_{66} & 0\\ 0 & A_{66}\end{bmatrix}\begin{bmatrix}\gamma_{\varphi z}\\ \gamma_{\theta z}\end{bmatrix}. \tag{10b}$$

The stiffness coefficients of the FGP spherical shell can be defined as follows:

$$(A_{ij},\ B_{ij},\ D_{ij}) = \int_{-h/2}^{h/2} Q_{ij}(z)(1,\ z,\ z^2)\mathrm{d}z. \tag{11}$$

Based on the aforementioned formulations, the strain energy of the FGP spherical shell is given as follows:

$$\begin{aligned} U = \frac{1}{2}\iiint_v &\begin{pmatrix} N_{\varphi\varphi}\varepsilon^0_{\varphi\varphi} + N_{\theta\theta}\varepsilon^0_{\theta\theta} + N_{\varphi\theta}\gamma^0_{\varphi\theta} + M_{\varphi\varphi}\kappa_{\varphi\varphi}\\ + M_{\theta\theta}\kappa_{\theta\theta} + M_{\varphi\theta}\kappa_{\varphi\theta} + Q_{\varphi z}\gamma_{\varphi z} + Q_{\theta z}\gamma_{\theta z}\end{pmatrix}\\ &\times RR_\varphi \mathrm{d}\varphi\mathrm{d}\theta\mathrm{d}z. \end{aligned} \tag{12}$$

Next, the kinetic energy can be written as follows:

$$\begin{aligned} T = \frac{1}{2}\int_{\varphi_0}^{\varphi_1}\int_0^{2\pi} &\{I_0[(\dot{u})^2 + (\dot{v})^2 + (\dot{w})^2] + 2I_1(\dot{u}\dot{\psi}_\varphi + \dot{v}\dot{\psi}_\theta)\\ &+ I_2[(\dot{\psi}_\varphi)^2 + (\dot{\psi}_\theta)^2]\}RR_\varphi \mathrm{d}\varphi\mathrm{d}\theta. \end{aligned} \tag{13}$$

In this work, the mathematical model of elastic boundary conditions is conducted through the virtual spring technique, and it can be expressed as follows:

$$U_{\mathrm{b}} = \int_c (k_{u,0}u^2 + k_{v,0}v^2 + k_{w,0}w^2 + k_{\varphi,0}\psi_x^2 + k_{\theta,0}\psi_\theta^2)RR_\varphi \mathrm{d}\theta|_{\varphi=0} + \int_c (k_{u,1}u^2 + k_{v,1}v^2 + k_{w,1}w^2 + k_{\varphi,1}\psi_x^2 + k_{\theta,1}\psi_\theta^2)RR_\varphi \mathrm{d}\theta|_{\varphi=\varphi_1-\varphi_0}, \tag{14}$$

where $k_{i,j}$ ($i = u, v, w, \varphi, \theta$ and $j = 0, 1$) are the virtual springs. To describe the continuity of shell segments, the potential energy is derived as follows:

$$U_{\mathrm{ss}} = \frac{1}{2}\int_0^{2\pi}\int_{-h/2}^{h/2} \begin{Bmatrix} k_u(u^i - u^{i+1})^2 + k_v(v^i - v^{i+1})^2 \\ + k_w(w^i - w^{i+1})^2 + k_\varphi(\psi_\varphi^i - \psi_\varphi^{i+1})^2 \\ + k_\theta(\psi_\theta^i - \psi_\theta^{i+1})^2 \end{Bmatrix} R_\varphi \mathrm{d}\theta \mathrm{d}z. \tag{15}$$

Therefore, the boundary and continuity conditions can be expressed by the potential energy equations as follows:

$$U_{\mathrm{BC}} = U_{\mathrm{b}} + U_{\mathrm{ss}}. \tag{16}$$

2.3 Admissible functions and solution procedure

To obtain a unified solution for the spherical shell, the displacements and rotations should be expanded as admissible displacement functions. The admissible functions should be suitable to different boundary conditions and can provide excellent convergence rates and accuracy. Chebyshev polynomials show great computational efficiency as a kind of admissible function. Therefore, the Chebyshev polynomials of the third kind are employed to build the discrete equations of the spherical shell. The recurrence formulations of the Chebyshev polynomials of the third kind are given as follows:

$$P_0(\varphi) = 1, \tag{17a}$$

$$P_1(\varphi) = \varphi, \tag{17b}$$

$$P_i(\varphi) = \frac{(2i-2)(2i\varphi(2i-2))}{2i^2(2i-2)}P_{i-1}(\varphi) - \frac{(i-1)^2}{i^2(2i-2)}P_{i-2}(\varphi), \tag{17c}$$

where $i = 2, 3, \ldots, N$.

The linear and rotational displacement components of the spherical shell can be rewritten as follows:

$$u = \sum_{m=0}^{M} U_m P_m(\varphi)\cos(n\theta)e^{i\omega t}, \tag{18a}$$

$$v = \sum_{m=0}^{M} V_m P_m(\varphi)\sin(n\theta)e^{i\omega t}, \tag{18b}$$

$$w = \sum_{m=0}^{M} W_m P_m(\varphi)\cos(n\theta)e^{i\omega t}, \tag{18c}$$

$$\psi_\varphi = \sum_{m=0}^{M} \psi_{\varphi m} P_m(\varphi)\cos(n\theta)e^{i\omega t}, \tag{18d}$$

$$\psi_\theta = \sum_{m=0}^{M} \psi_{\theta m} P_m(\varphi)\cos(n\theta)e^{i\omega t}. \tag{18e}$$

The Lagrange function of the spherical shell can be expressed as follows:

$$L = U + U_{\mathrm{BC}} - T. \tag{19}$$

The derivatives of the Lagrange function with respect to the unknown coefficients are calculated, making the results equal to zero, and then the expression is obtained as follows:

$$\frac{\partial L}{\partial \vartheta} = 0 \quad \vartheta = U_m,\ V_m,\ W_m,\ \psi_{\varphi m},\ \psi_{\theta m}. \tag{20}$$

Substituting equations (12)–(19) into equation (20), the eigenvalue equation is obtained as follows:

$$(\boldsymbol{K} - i\omega\boldsymbol{C} - \omega^2\boldsymbol{M})\boldsymbol{P} = \boldsymbol{F}, \tag{21}$$

where $\boldsymbol{K}$ represents the stiffness matrix, $\boldsymbol{M}$ indicates the mass matrix, $\boldsymbol{C}$ is the damping matrix, $\boldsymbol{P}$ is the unknown coefficient vector, and $\boldsymbol{F}$ denotes the external force vector. Then, the spherical shell's natural frequency and mode shape can be obtained by solving equation (21).

For the forced vibration of the spherical shell, four kinds of loading pulses are considered as follows:

Rectangular

$$f_r(t) = \begin{cases} 1, & 0 \le t \le \tau, \\ 0, & \text{otherwise}, \end{cases} \tag{22a}$$

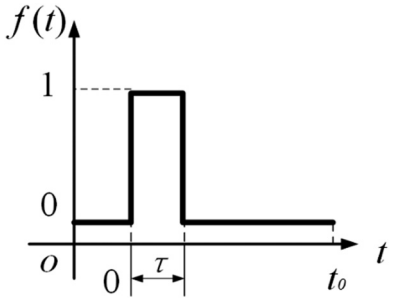

Triangular

$$f_t(t) = \begin{cases} \frac{2t}{\tau}, & 0 \le t \le \frac{\tau}{2}, \\ 1 - \frac{2}{\tau}\left(t - \frac{\tau}{2}\right), & \frac{\tau}{2} \le t \le \tau, \\ 0, & \text{otherwise}, \end{cases} \tag{22b}$$

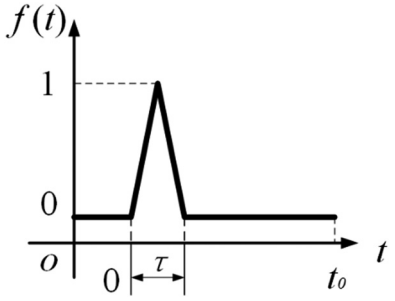

Half-sine

$$f_h(t) = \begin{cases} \sin\left(\frac{\pi t}{\tau}\right), & 0 \le t \le \tau, \\ 0, & \text{otherwise}, \end{cases} \tag{22c}$$

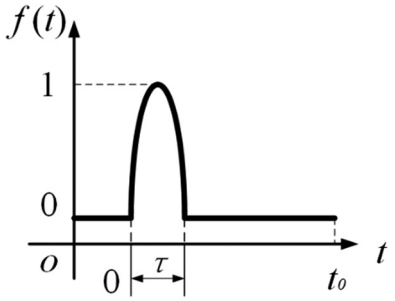

Exponential

$$f_e(t) = \begin{cases} e^{-\xi t}, & 0 \le t \le \tau, \\ 0, & \text{otherwise}, \end{cases} \tag{22d}$$

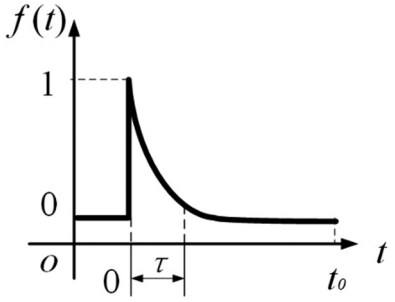

where τ and t are the pulse width and the time variable, respectively. The expression of external force loading is $F_i(t) = q_0 f_i(t)$, where i takes r, t, h, or e. Furthermore, the governing equation of forced vibration of the spherical shell is given as follows:

$$\boldsymbol{M}\ddot{\boldsymbol{u}} + \boldsymbol{C}\dot{\boldsymbol{u}} + \boldsymbol{k}\boldsymbol{u} = \boldsymbol{F}, \tag{23}$$

where $\ddot{\boldsymbol{u}}$, $\dot{\boldsymbol{u}}$, and $\boldsymbol{u}$ are the acceleration, velocity, and displacement vectors, respectively. Based on the aforementioned formulations, the forced vibration characteristics of the spherical shell can be calculated by utilizing the Newmark-β approach as follows:

$$\dot{\boldsymbol{u}}_{t+\Delta t} = \dot{\boldsymbol{u}}_t + [(1-\gamma)\ddot{\boldsymbol{u}}_t + \gamma\ddot{\boldsymbol{u}}_{t+\Delta t}]\Delta t, \tag{24a}$$

$$\boldsymbol{u}_{t+\Delta t} = \boldsymbol{u}_t + \dot{\boldsymbol{u}}_t\Delta t + \left[\left(-\frac{1}{2} - \beta\right)\ddot{\boldsymbol{u}}_t + \beta\ddot{\boldsymbol{u}}_{t+\Delta t}\right]\Delta t^2, \tag{24b}$$

where γ is set as 1/2, and β is set as 1/4.

3 Analysis and discussion

In this section, the primary goal is to investigate the factors, which can influence the vibration characteristics of the FGP spherical shell. To obtain a satisfactory converged solution, the correlative parameters should be determined first. It is observed that the present literature [37] has

Table 1: Comparison of the first four frequencies $\Omega = \omega R\sqrt{\rho_1/E_1}/h$ of Type 1 FGP spherical shell with various boundary conditions (R = 2 m, φ_0 = 30°, φ_1 = 90°, h = 0.1 m, e_0 = 0.2, ρ_1 = 7,850 kg/m^3, E_1 = 200 GPa, μ = 0.3)

e_0	Mode	Boundary conditions								
		CC			SS			CF		
		Ram and Babu [11]	Present	Error (%)	Ram and Babu [11]	Present	Error (%)	Ram and Babu [11]	Present	Error (%)
0.2	1	21.15	21.15	0.00	18.11	18.11	0.00	2.251	2.246	0.24
	2	21.68	21.68	0.01	19.95	19.95	0.02	3.205	3.199	0.20
	3	21.77	21.77	0.02	20.95	20.94	0.03	4.820	4.814	0.12
	4	22.39	22.37	0.08	21.35	21.35	0.00	5.691	5.678	0.22
0.4	1	20.38	20.38	0.02	18.30	18.30	0.01	2.167	2.162	0.21
	2	20.88	20.88	0.00	19.14	19.13	0.07	3.082	3.075	0.22
	3	20.98	20.97	0.03	20.22	20.22	0.01	4.647	4.642	0.12
	4	21.55	21.53	0.08	20.61	20.61	0.01	5.472	5.459	0.23
0.6	1	19.55	19.55	0.01	17.38	17.38	0.00	2.068	2.063	0.24
	2	20.01	20.01	0.02	18.23	18.22	0.04	2.916	2.910	0.22
	3	20.15	20.14	0.03	19.46	19.45	0.03	4.463	4.458	0.12
	4	20.58	20.56	0.09	19.82	19.82	0.01	5.177	5.165	0.23

accomplished the convergence study of the spherical shell. To simplify the article structure, the number of segments and truncations are set as 5 and 8, and the coupling parameters are equal to 10^{14}. Besides, the different boundary conditions at each edge of the spherical shell (i = 0, 1) are achieved by setting the spring stiffness values as follows: Completely free (F): $k_{u,i} = k_{v,i} = k_{w,i} = k_{\varphi,i} = k_{\theta,i} = 0$; Completely clamped (C): $k_{u,i} = k_{v,i} = k_{w,i} = k_{\varphi,i} = k_{\theta,i} = 10^{14}$; Simply supported (S): $k_{u,i} = k_{v,i} = k_{w,i} = k_{\theta,i} = 10^{14}$, $k_{\varphi,i} = 0$; Elastic constrain 1 (E1): $k_{u,i} = k_{v,i} = 10^8$, $k_{w,i} = k_{\varphi,i} = k_{\theta,i} = 10^{14}$; Elastic constrain 2 (E2): $k_{u,i} = k_{v,i} = k_{\varphi,i} = k_{\theta,i} = 10^{14}$, $k_{w,i} = 10^8$; and Elastic constrain 3 (E3): $k_{u,i} = k_{v,i} = k_{w,i} = 10^8$; $k_{\varphi,i} = k_{\theta,i} = 10^{14}$.

3.1 Free vibration

Before conducting the parametric study, the correctness of the results obtained from the proposed method should be verified by comparing it with the published literature. The relevant parameters of the FGP spherical shell are set as follows: R = 2 m, φ_0 = 30°, φ_1 = 90°, h = 0.1 m, ρ_1 = 7,850 kg/m^3, E_1 = 200 GPa, and μ = 0.3. If there is no special reminder in the following study, the parameters remain unchanged. The dimensionless frequency is defined as follows: $\Omega = \omega R\sqrt{\rho_1/E_1}/h$. Through a comparison study, Table 1 illustrates that the results calculated by the proposed model are in good agreement with

Table 2: Frequencies $\Omega = \omega R\sqrt{\rho_1/E_1}/h$ of the FGP spherical shell considering different classical boundary conditions and porosity distribution (R = 2 m, φ_0 = 30°, φ_1 = 150°, h = 0.1 m, e_0 = 0.2, ρ_1 = 2,702 kg/m^3, E_1 = 70 GPa, μ = 0.3)

n	m	Type 1			Type 2			Type 3		
		CS	CF	SF	CS	CF	SF	CS	CF	SF
0	1	13.593	2.300	1.999	13.551	2.292	1.975	13.328	2.249	1.959
	2	13.771	13.342	13.026	13.761	13.329	12.990	13.508	13.085	12.778
	3	19.253	17.797	17.585	19.193	17.767	17.547	18.843	17.446	17.240
	4	21.054	19.119	19.032	20.892	19.070	18.973	20.521	18.726	18.638
1	1	15.962	3.643	3.636	15.943	3.568	3.560	15.660	3.495	3.487
	2	18.246	16.598	16.589	18.217	16.573	16.560	17.886	16.275	16.265
	3	20.627	18.611	18.541	20.553	18.563	18.504	20.167	18.227	18.166
	4	22.568	21.097	20.832	22.388	20.966	20.729	21.969	20.581	20.340
2	1	17.462	9.450	9.450	17.436	9.274	9.274	17.125	9.088	9.088
	2	19.394	17.680	17.679	19.336	17.643	17.642	18.984	17.326	17.325
	3	21.507	19.752	19.722	21.391	19.665	19.644	20.987	19.308	19.283
	4	24.369	22.258	22.066	24.148	22.077	21.916	23.676	21.667	21.495

Table 3: Frequencies $\Omega = \omega R\sqrt{\rho_1/E_1}/h$ of the FGP spherical shell considering different elastic boundary conditions and porosity distribution (R = 2 m, φ_0 = 30°, φ_1 = 150°, h = 0.1 m, e_0 = 0.2, ρ_1 = 2,702 kg/m^3, E_1 = 70 GPa, μ = 0.3)

n	*m*	Type 1			Type 2			Type 3		
		E2E2	E3E3	E1E2	E2E2	E3E3	E1E2	E2E2	E3E3	E1E2
0	1	13.021	2.594	3.552	13.014	2.593	3.548	12.777	2.549	3.485
	2	13.484	3.293	13.150	13.478	3.289	13.138	13.232	3.231	12.898
	3	19.117	15.345	17.961	19.081	15.333	17.919	18.736	15.058	17.597
	4	19.565	18.117	20.019	19.497	18.084	19.937	19.146	17.760	19.572
1	1	15.843	6.815	10.589	15.827	6.781	10.547	15.543	6.659	10.354
	2	18.282	7.943	17.526	18.248	7.899	17.481	17.919	7.754	17.166
	3	20.751	17.931	19.234	20.661	17.881	19.176	20.285	17.559	18.828
	4	21.887	19.399	22.403	21.776	19.346	22.261	21.376	18.992	21.850
2	1	17.441	13.303	16.012	17.415	13.217	15.959	17.103	12.974	15.671
	2	19.409	13.990	18.473	19.345	13.885	18.409	18.996	13.628	18.076
	3	21.596	18.687	20.802	21.466	18.608	20.673	21.072	18.270	20.294
	4	24.288	21.320	23.924	24.079	21.161	23.691	23.630	20.770	23.248

the existing data, and the maximum error is less than 1%. Therefore, the proposed model can be used to investigate the vibration behaviors of the spherical shell.

Tables 2 and 3 investigate the effect of boundary conditions and porosity distributions on the vibration behaviors of the FGP spherical shell. Through these tables, it is

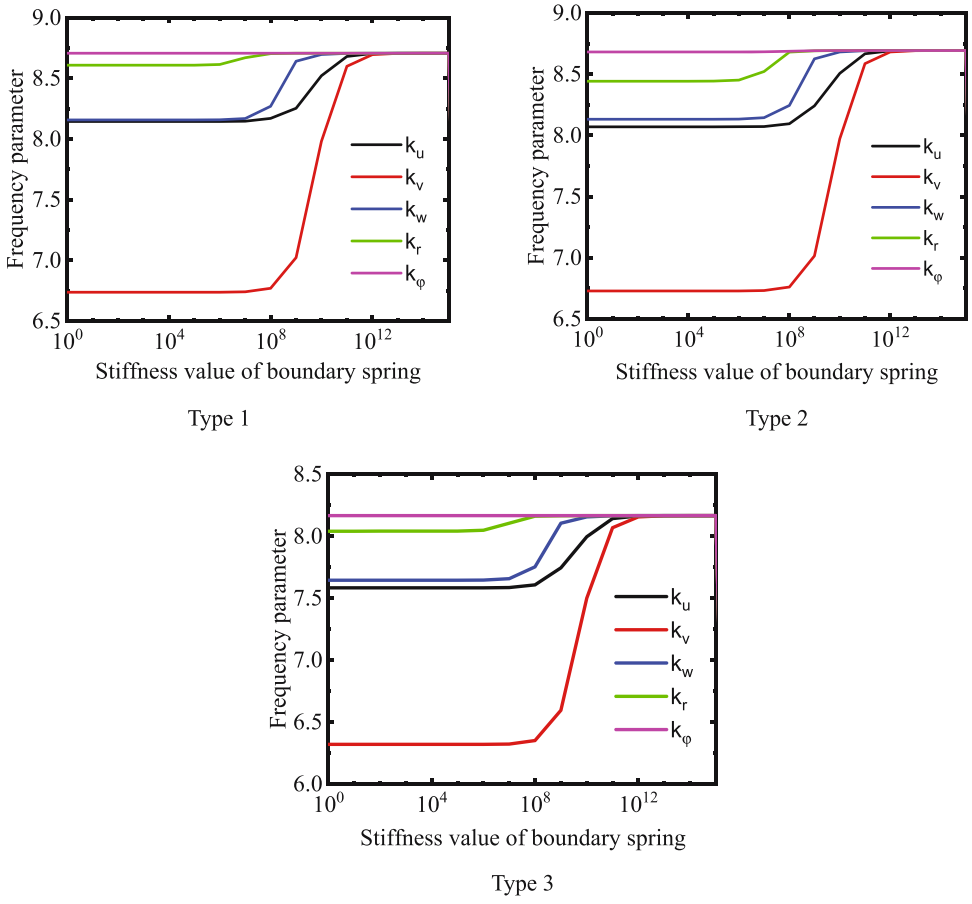

Figure 2: Effect of boundary stiffness on dynamic characteristics of FGP spherical shell (R = 2 m, φ_0 = 30°, φ_1 = 150°, h = 0.15 m, e_0 = 0.5).

Table 4: Frequencies $\Omega = \omega R\sqrt{\rho_1/E_1}/h$ of the FGP spherical shell considering different classical-elastic boundary conditions and porosity distribution (R = 2 m, φ_0 = 30°, φ_1 = 150°, h = 0.1 m, e_0 = 0.2, ρ_1 = 2,702 kg/m^3, E_1 = 70 GPa, μ = 0.3)

Porosity distribution	Mode number		Boundary conditions					
	n	*m*	C-E1	C-E2	C-E3	S-E1	S-E2	S-E3
Type 1	1	1	3.779	13.318	3.627	3.592	13.135	3.441
		2	13.766	13.804	13.472	13.418	13.627	13.144
		3	18.538	19.209	18.165	18.265	19.059	17.911
	2	1	10.589	15.906	7.287	10.587	15.895	7.284
		2	17.586	18.284	17.037	17.583	18.243	17.029
		3	19.340	20.765	18.895	19.137	20.622	18.776
Type 2	1	1	3.771	13.308	3.621	3.575	13.112	3.427
		2	13.743	13.792	13.456	13.371	13.605	13.105
		3	18.479	19.162	18.124	18.195	19.023	17.861
	2	1	10.547	15.891	7.250	10.546	15.875	7.246
		2	17.543	18.249	17.008	17.538	18.215	16.995
		3	19.267	20.671	18.841	19.083	20.550	18.736
Type 3	1	1	3.703	13.065	3.557	3.524	12.887	3.379
		2	13.490	13.539	13.210	13.153	13.368	12.891
		3	18.143	18.816	17.796	17.879	18.675	17.551
	2	1	10.354	15.606	7.118	10.353	15.593	7.114
		2	17.227	17.920	16.702	17.224	17.884	16.692
		3	18.916	20.294	18.499	18.732	20.165	18.393

obvious that the largest frequency appears in the clamped boundary condition, and the frequency parameters under the elastic constraints change irregularly relative to the stiffness value. To clarify this phenomenon, the effect of boundary parameters on the free vibration of the FGP spherical shell is further investigated in Figure 2. The clamped condition and elastic constraints, respectively, are employed at $\varphi = \varphi_0$ and $\varphi = \varphi_1$. In this work, only one of the spring types is changed, and others remain at 10^{14}. It is easy to discover that the frequencies increase rapidly with the increase of the stiffness of boundary conditions, and sufficiently converged solutions are obtained when the stiffness value exceeds 10^{12}. Based on this find, it can be considered that the boundary condition beyond the threshold is clamped boundary. Hence, the vibration behaviors can be regulated by changing the stiffness value. It is also directly observed that the effect of linear springs is significant to the fundamental frequencies, and the rotational springs are unnoticeable. Furthermore, Table 4 shows the fundamental frequencies of the FGP spherical shell with

Table 5: Frequencies $\Omega = \omega R\sqrt{\rho_1/E_1}/h$ of the C–C FGP spherical shell concerning various porosity ratios and porosity distribution (R = 2 m, φ_0 = 30°, φ_1 = 150°, h = 0.1 m, ρ_1 = 2,702 kg/m^3, E_1 = 70 GPa, μ = 0.3)

Porosity distribution	*n*	*m*	e_0								
			0.1	0.2	0.3	0.4	0.5	0.6	0.7	0.8	0.9
Type 1	1	1	13.950	13.717	13.478	13.235	12.991	12.751	12.530	12.363	12.362
		2	14.236	14.010	13.780	13.547	13.314	13.089	12.886	12.742	12.777
	2	1	16.245	15.975	15.699	15.418	15.136	14.860	14.606	14.414	14.419
		2	18.584	18.286	17.982	17.674	17.367	17.069	16.801	16.610	16.653
Type 2	1	1	13.947	13.712	13.470	13.223	12.974	12.728	12.499	12.320	12.300
		2	14.223	13.982	13.734	13.478	13.217	12.956	12.705	12.492	12.418
	2	1	16.238	15.961	15.675	15.383	15.088	14.795	14.521	14.301	14.267
		2	18.567	18.250	17.922	17.586	17.243	16.900	16.571	16.298	16.219
Type 3	1	1	13.828	13.460	13.068	12.646	12.187	11.681	11.110	10.442	9.605
		2	14.101	13.726	13.326	12.895	12.428	11.912	11.329	10.648	9.795
	2	1	16.102	15.674	15.217	14.725	14.191	13.602	12.937	12.159	11.185
		2	18.411	17.921	17.399	16.837	16.226	15.552	14.792	13.903	12.788

Table 6: Frequencies $\Omega = \omega R\sqrt{\rho_1/E_1}/h$ of the C–C FGP spherical shell concerning different thickness ratios and porosity distribution (R = 2 m, φ_0 = 30°, φ_1 = 150°, h = 0.1 m, ρ_1 = 2,702 kg/m^3, E_1 = 70 GPa, μ = 0.3)

Porosity distribution	h/R	e_0								
		0.1	0.2	0.3	0.4	0.5	0.6	0.7	0.8	0.9
Type 1	0.02	33.118	32.568	32.005	31.433	30.857	30.294	29.776	29.385	29.393
	0.05	13.562	13.341	13.115	12.886	12.656	12.432	12.228	12.078	12.094
	0.1	7.040	6.926	6.806	6.685	6.563	6.444	6.334	6.251	6.253
	0.15	4.735	4.657	4.577	4.495	4.413	4.333	4.259	4.204	4.205
	0.2	3.573	3.514	3.454	3.392	3.331	3.270	3.215	3.173	3.175
Type 2	0.02	33.078	32.484	31.869	31.236	30.588	29.935	29.302	28.751	28.507
	0.05	13.535	13.283	13.021	12.750	12.471	12.186	11.903	11.645	11.496
	0.1	7.017	6.881	6.739	6.590	6.436	6.275	6.112	5.957	5.847
	0.15	4.735	4.656	4.574	4.491	4.406	4.321	4.204	4.080	3.981
	0.2	3.574	3.516	3.456	3.394	3.332	3.270	3.210	3.155	3.061
Type 3	0.02	32.828	31.954	31.022	30.020	28.932	27.730	26.374	24.789	22.801
	0.05	13.439	13.082	12.700	12.290	11.844	11.353	10.798	10.148	9.335
	0.1	6.972	6.787	6.589	6.376	6.145	5.890	5.602	5.265	4.843
	0.15	4.693	4.568	4.435	4.292	4.136	3.965	3.771	3.544	3.260
	0.2	3.542	3.447	3.347	3.239	3.121	2.992	2.845	2.674	2.460

the hybrid boundary of classical-elastic conditions. The parametric study as mentioned earlier is unpublished, and it could provide future worker standard data as a reference.

Table 5 shows the frequencies of the FGP spherical shell under the C–C boundary with different porosity coefficients. From the results shown in Table 5, it is noteworthy that frequencies gradually decrease with the increase of porosity coefficient, whatever be the type of porosity distribution. This is because the internal pore leads to the structural stiffness decrease. It can be seen that the FGP porosity distributions have a significant effect on the frequencies. Besides, the growth of the porosity coefficient has less effect on the FGP spherical shell with porosity distribution $T-1$. The reason is that the symmetric distribution of porosity is hypersensitive to the change in the size of porosity. Therefore, the porosity distribution $T-1$ has better stability under the variation of the porosity coefficient. A creditable explanation is that the porosity

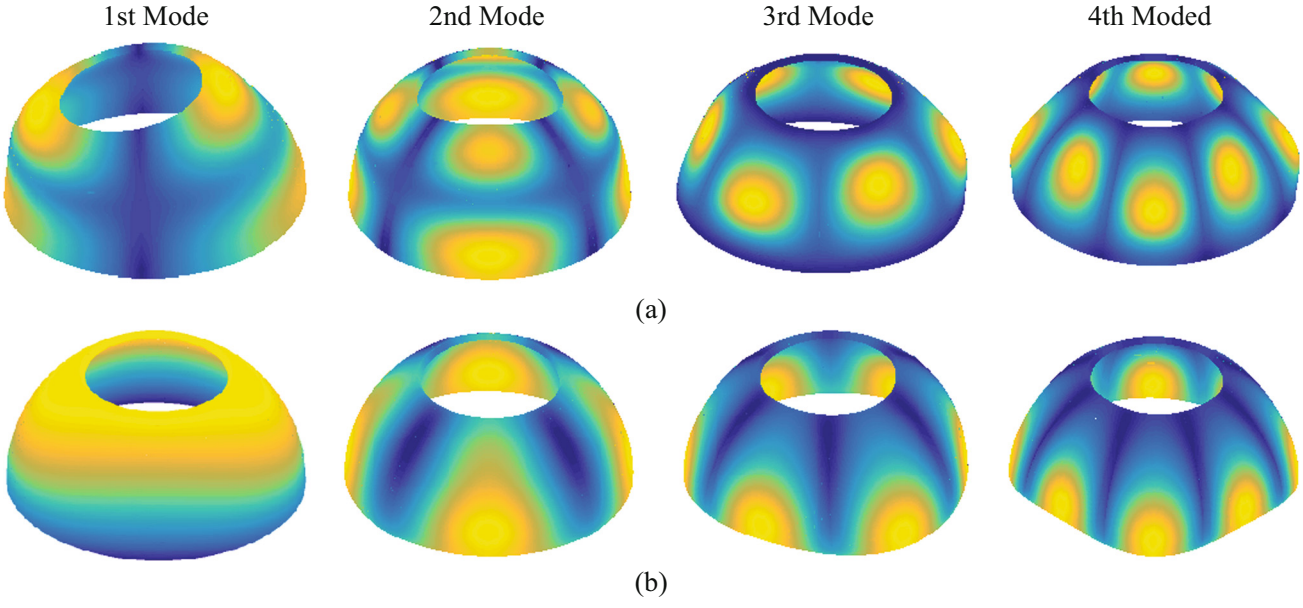

Figure 3: First four mode shapes of FGP spherical shell under different boundary conditions (Type 1, R = 2 m, φ_0 = 30°, φ_1 = 90°, h = 0.1 m, e_0 = 0.2). (a) E2–E2 and (b) E3–E3.

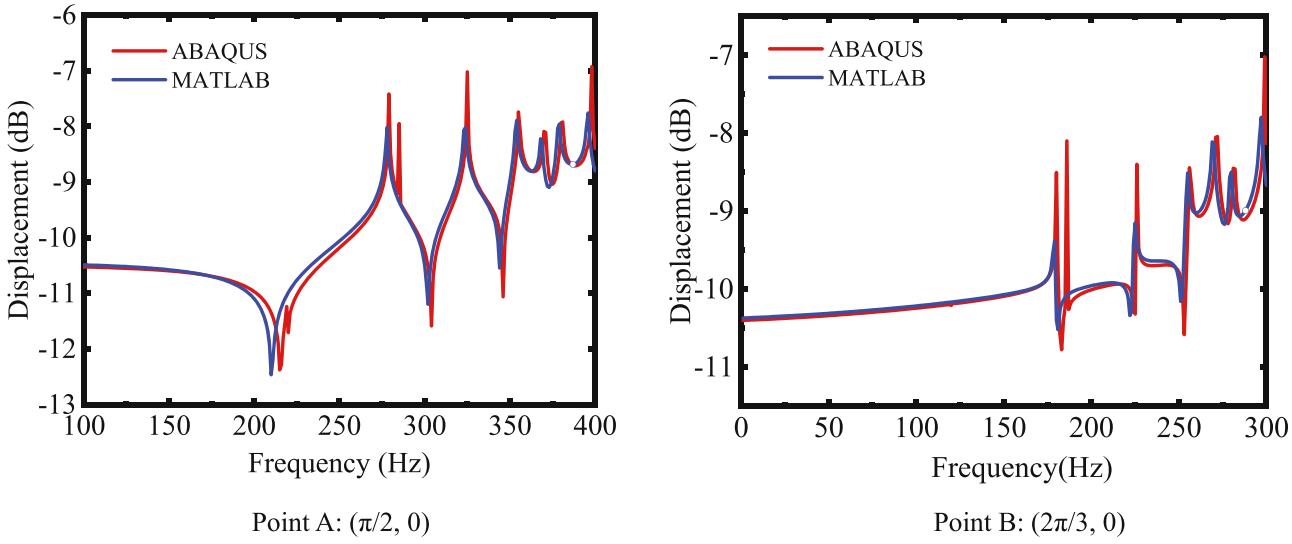

Figure 4: Comparison of both proposed method and ABAQUS software on steady response of T-1 FGP spherical shell (R = 2 m, φ_0 = 30°, φ_1 = 150°, h = 0.1 m, e_0 = 0.2, load position: (π/2, 0), f = 0–400 Hz, Δf = 2 Hz, CC boundary condition).

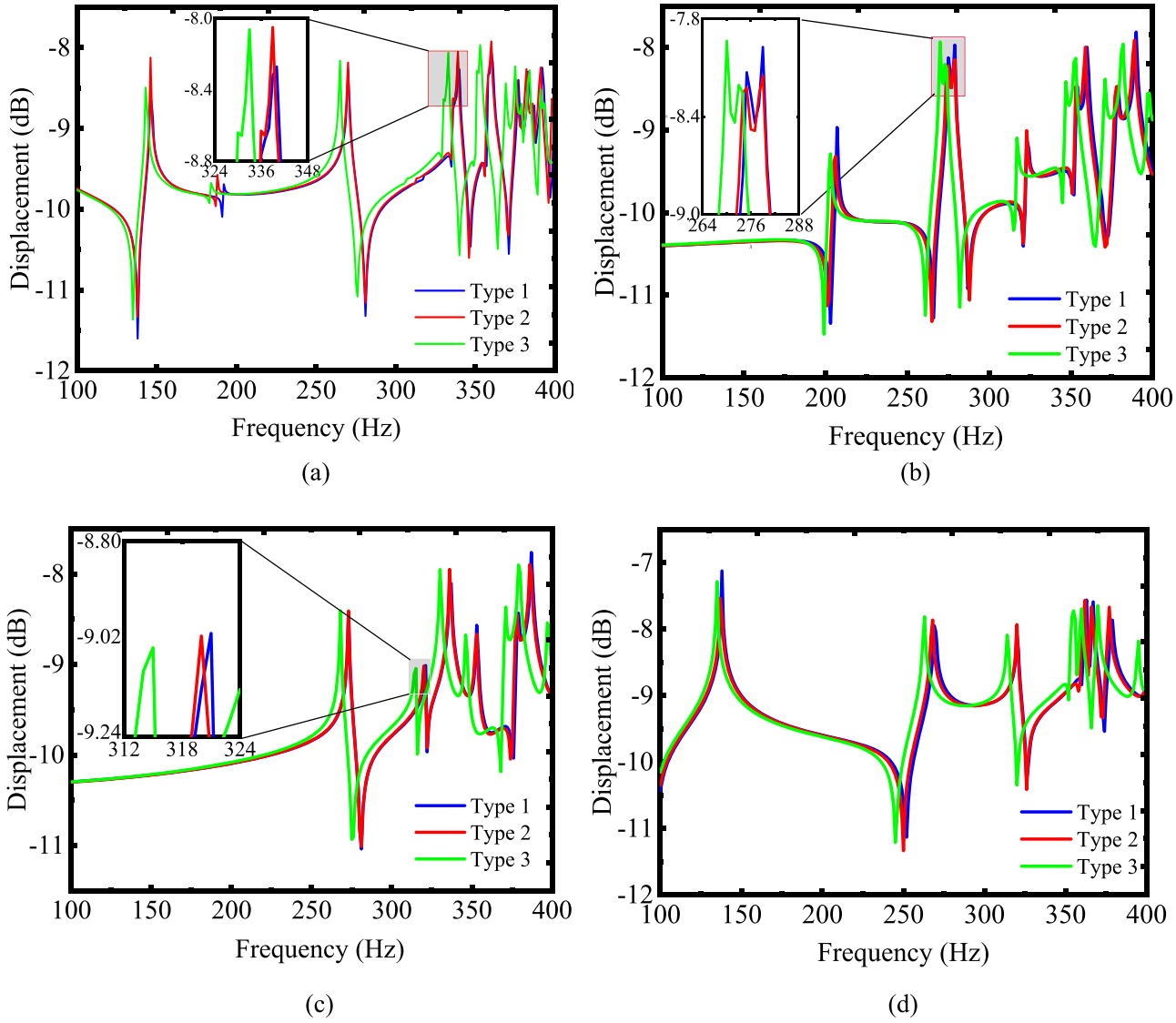

Figure 5: Effect of boundary conditions and porous types on steady response of FGP spherical shell (R = 2 m, φ_0 = 30°, φ_1 = 150°, h = 0.1 m, e_0 = 0.2, load position: (π/2, 0), observation location: (2π/3, 0), f = 0 Hz~400 Hz, Δf = 2 Hz). (a) C–F, (b) C–S, (c) E2–E2, and (d) E4–E4.

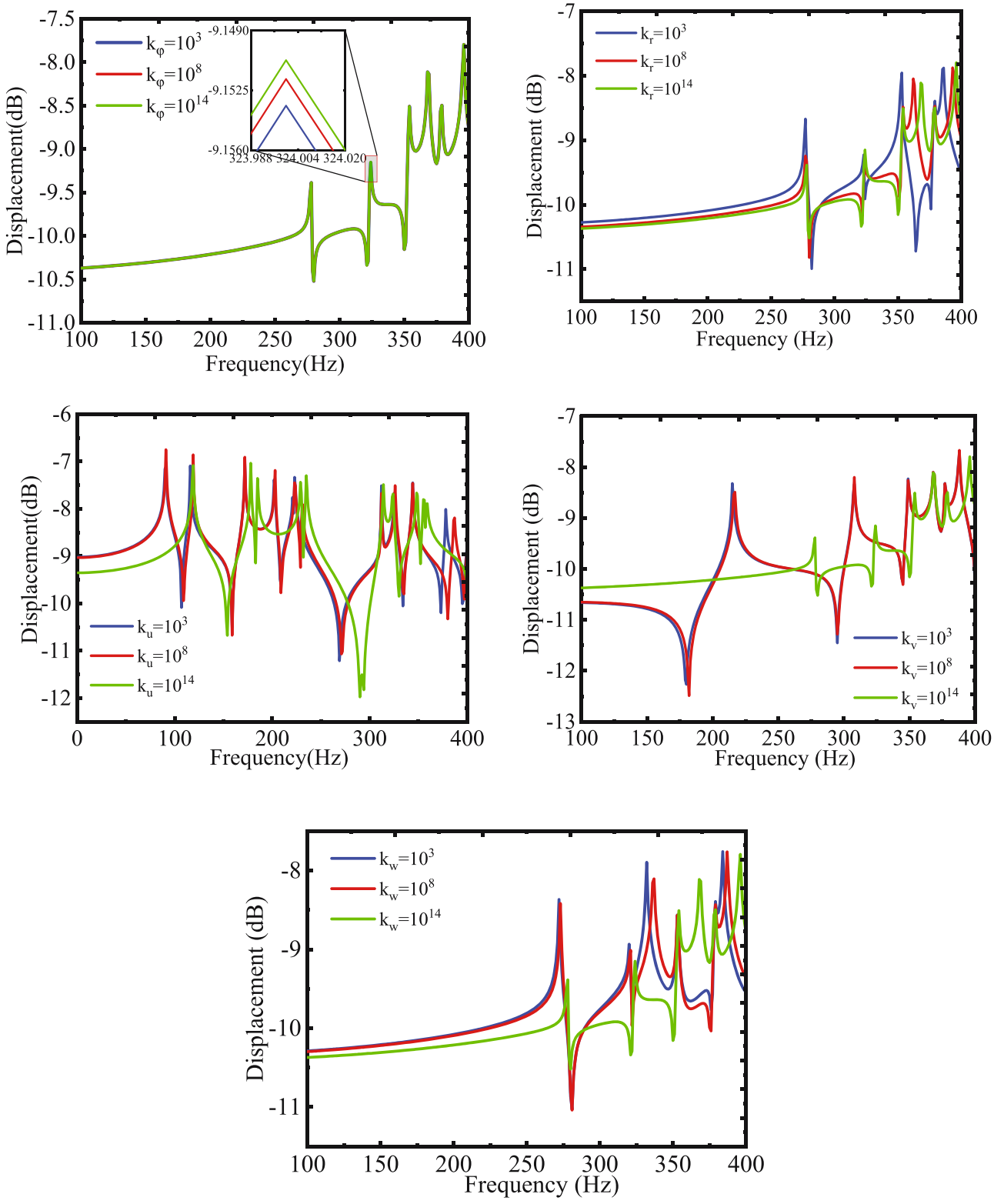

Figure 6: Effect of boundary stiffness coefficient on steady response of T-3 FGP spherical shell (R = 2 m, φ_0 = 30°, φ_1 = 150°, h = 0.1 m, e_0 = 0.2, load position: (π/2, 0), observation location: (2π/3, 0), f = 0–400 Hz, Δf = 2 Hz).

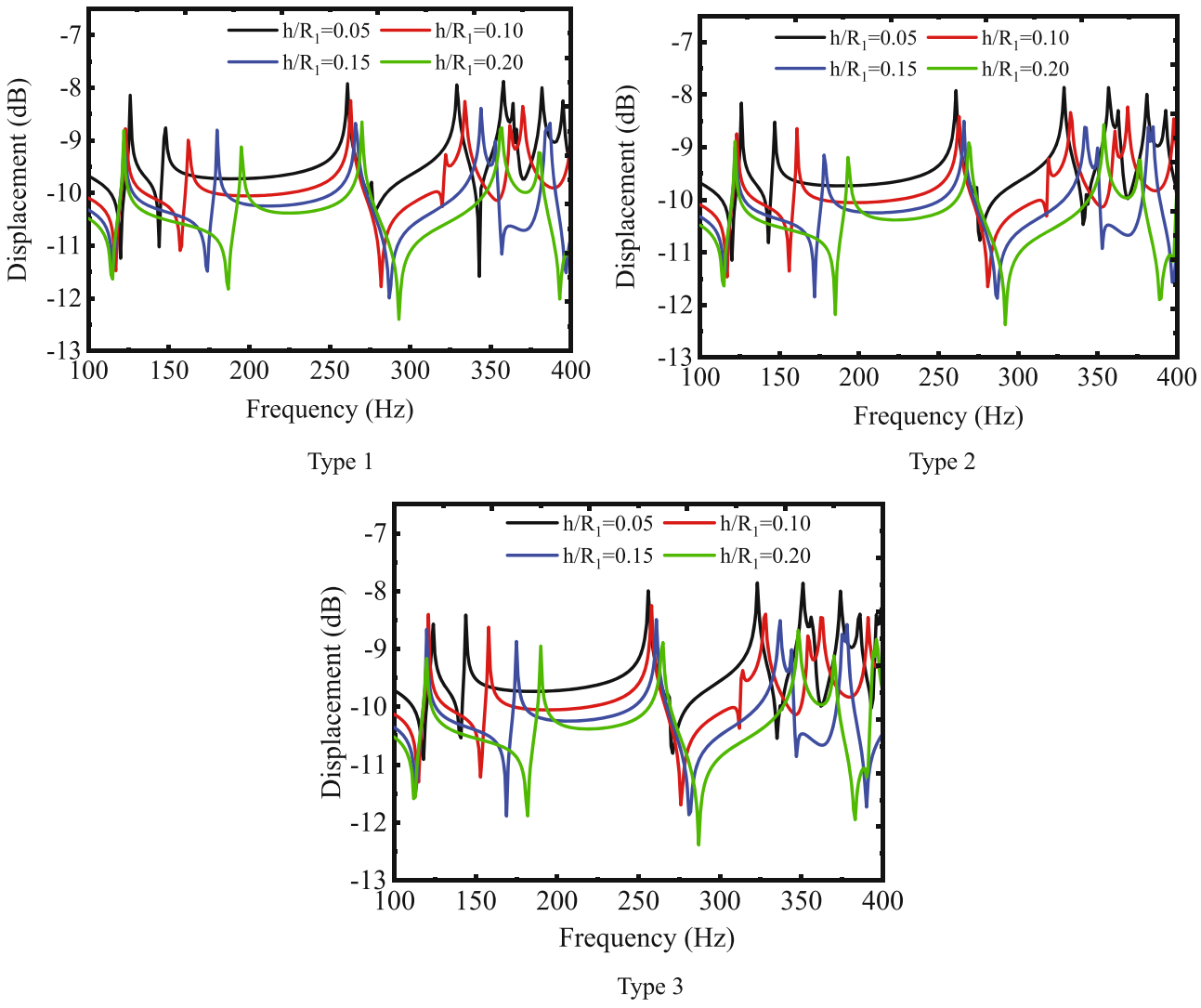

Figure 7: Effect of thickness ratio on steady response of the FGP spherical shell (R = 2 m, φ_0 = 30°, φ_1 = 150°, e_0 = 0.2, load position: (π/2, 0), observation location: (2π/3, 0), f = 0–400 Hz, Δf = 2 Hz, E2–E3 boundary condition).

distribution $T-1$ has higher stiffness than the others. In other words, the FGP spherical shell with porosity distribution $T-1$ can achieve the best mechanical performance and possess the highest dimensionless frequencies.

Table 6 shows the frequencies of the FGP spherical shell under the C–C boundary with various thickness–radius ratios. It is worth noting that the frequencies drop with the increase of the thickness–radius ratio. The result is because the value of the stiffness matrix grows with the increase of thickness–radius ratio. This finding suggests that the higher thickness ratios of the FGP spherical shell should be selected to improve the structural stability. To better understand the vibration behavior, the first four mode shapes of the FGP spherical shell with different boundary conditions are displayed in Figure 3.

3.2 Forced vibration

After the dynamic analysis of the FGP spherical shell, the forced vibration response is investigated in the following study. In this section, the steady-state and transient responses of the FGP spherical shell are discussed in detail.

3.2.1 Steady-state response

The validity of the approach proposed in this work needs to be studied before carrying out the relevant research. Figure 4 shows the comparison study of the proposed and finite element modeling (FEM) methods. The loading pulse can be further expressed as $f_w = \bar{f}_w \delta(\varphi - \varphi_0)\delta(\theta - \theta_0)$, and it is

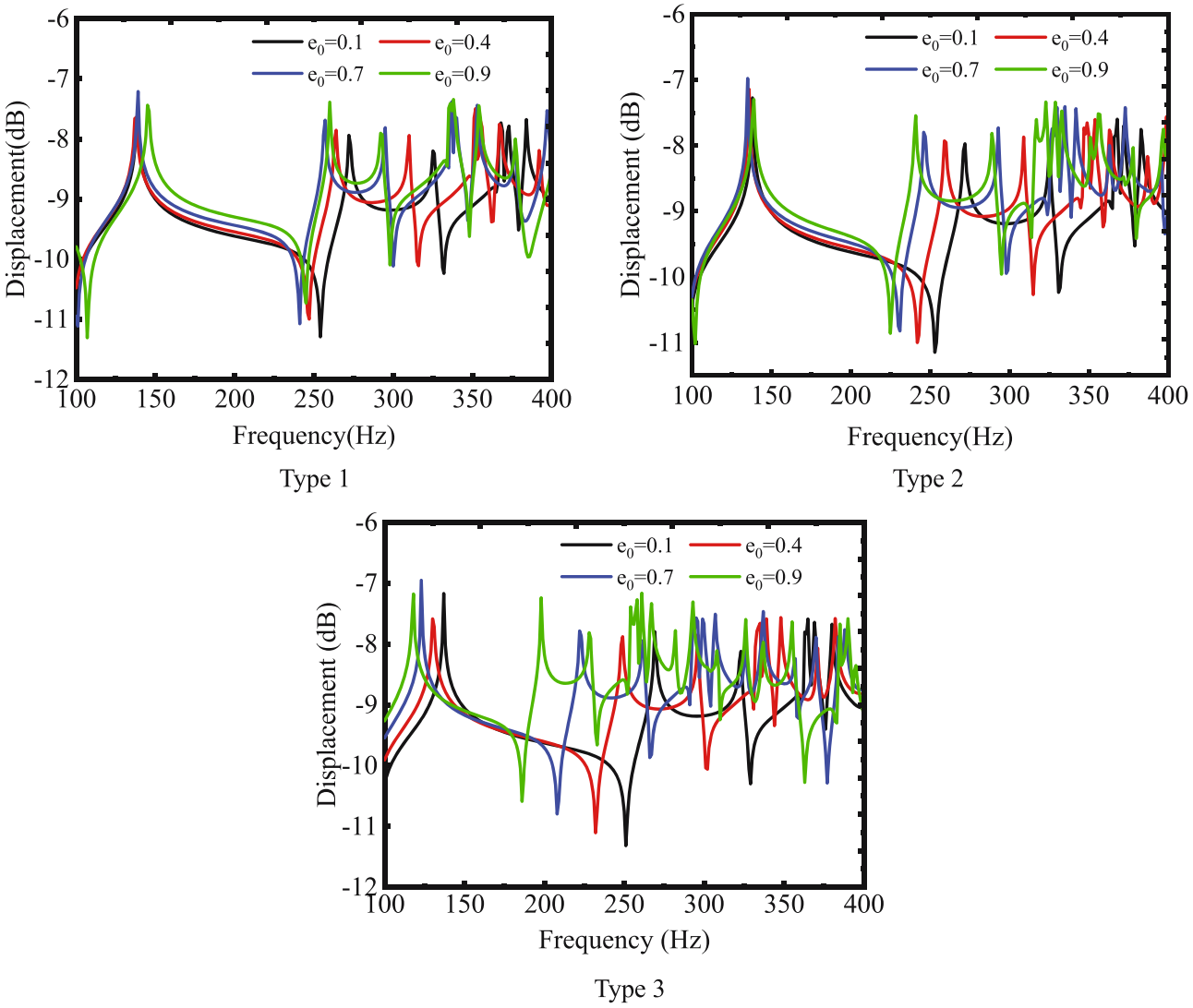

Figure 8: Effect of porosity ratios on steady response of FGP conical shell (R = 2 m, h = 0.1 m, φ_0 = 30°, φ_1 = 150°, load position: (π/2, 0), observation location: (2π/3, 0), f = 0–400 Hz, Δf = 2 Hz, S–S boundary condition).

point loading with an amplitude of −1N. The geometric parameters are set as R = 2 m, φ_0 = 30°, φ_1 = 150°, h = 0.1 m, and e_0 = 0.2. The load position is $\varphi = \pi/2$, $\theta = 0$, and two observed points are constructed: $A(\pi/2,\ 0)$ and $B(2\pi/3,\ 0)$. The sweep frequency range is f = 0–400 Hz, Δf = 2 Hz. The boundary condition is the C–C boundary. From Figure 4, it can be seen that the result obtained from the proposed approach is consistent with the FEM result. Hence, the correctness of the proposed model is verified, and based on the verification, the following investigation is presented.

Figure 5 illustrates the effect of boundary conditions on steady-state response. This figure illustrates that the boundary conditions of the FGP spherical shell have a direct effect on the steady-state response. For example, in the specific frequency range, the steady-state response curve appears with eight peaks of the wave under the C–F boundary but six peaks of the wave under the E4–E4 boundary. It can be attributed that the spring matrix of the FGP spherical shell is different under different boundary conditions.

Figure 6 carries out the relevant numerical analysis to further investigate the effect of the boundary spring parameters on the steady-state response of the FGP spherical shell. In this case, the variable of the boundary spring is set to only one by taking 10^3, 10^8, or 10^{14}, and others are constantly equal to 10^{14}. Through Figure 6, it is apparent that the linear springs affect the steady-state response more remarkably than the rotational springs, and the finding from forced vibration is similar to the free vibration.

Figure 7 investigates the effect of the thickness coefficient on the steady-state response. From the data in Figure 7, it is worth noting that the growth of the thickness ratio leads to the decline of the steady-state response peak, and the peak of

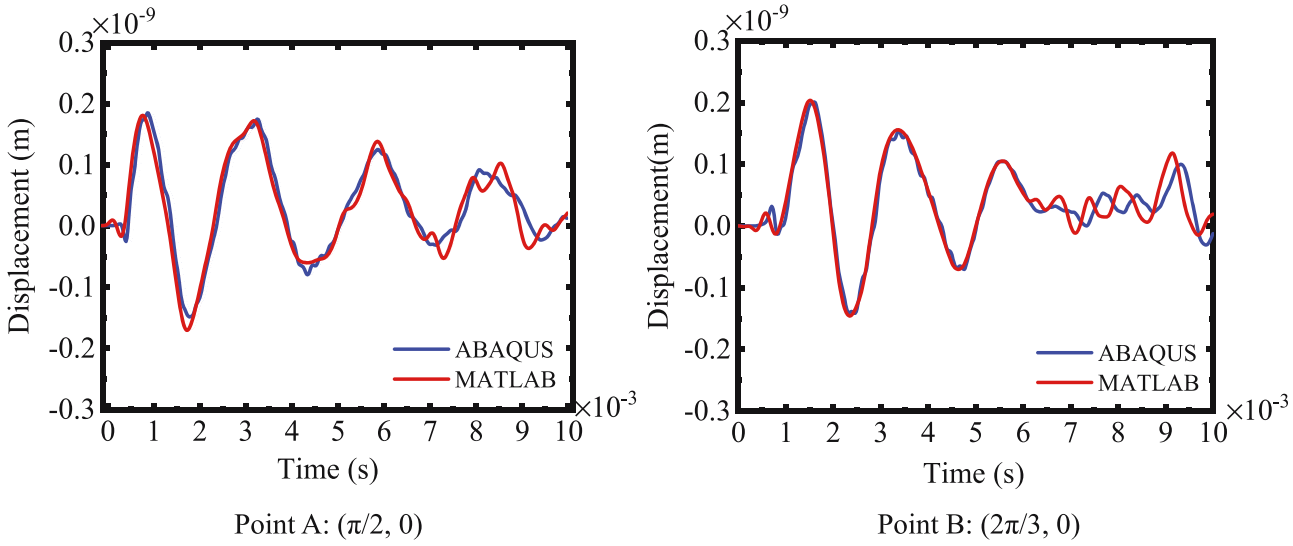

Figure 9: Comparison of both proposed method and ABAQUS software on transient response of T-1 FGP spherical shell (R = 2 m, φ_0 = 30°, φ_1 = 150°, h = 0.1 m, e_0 = 0.2, load position: (π/2, 0), $t = \tau$ = 10 ms, Δt = 0.01 ms, C–C boundary condition).

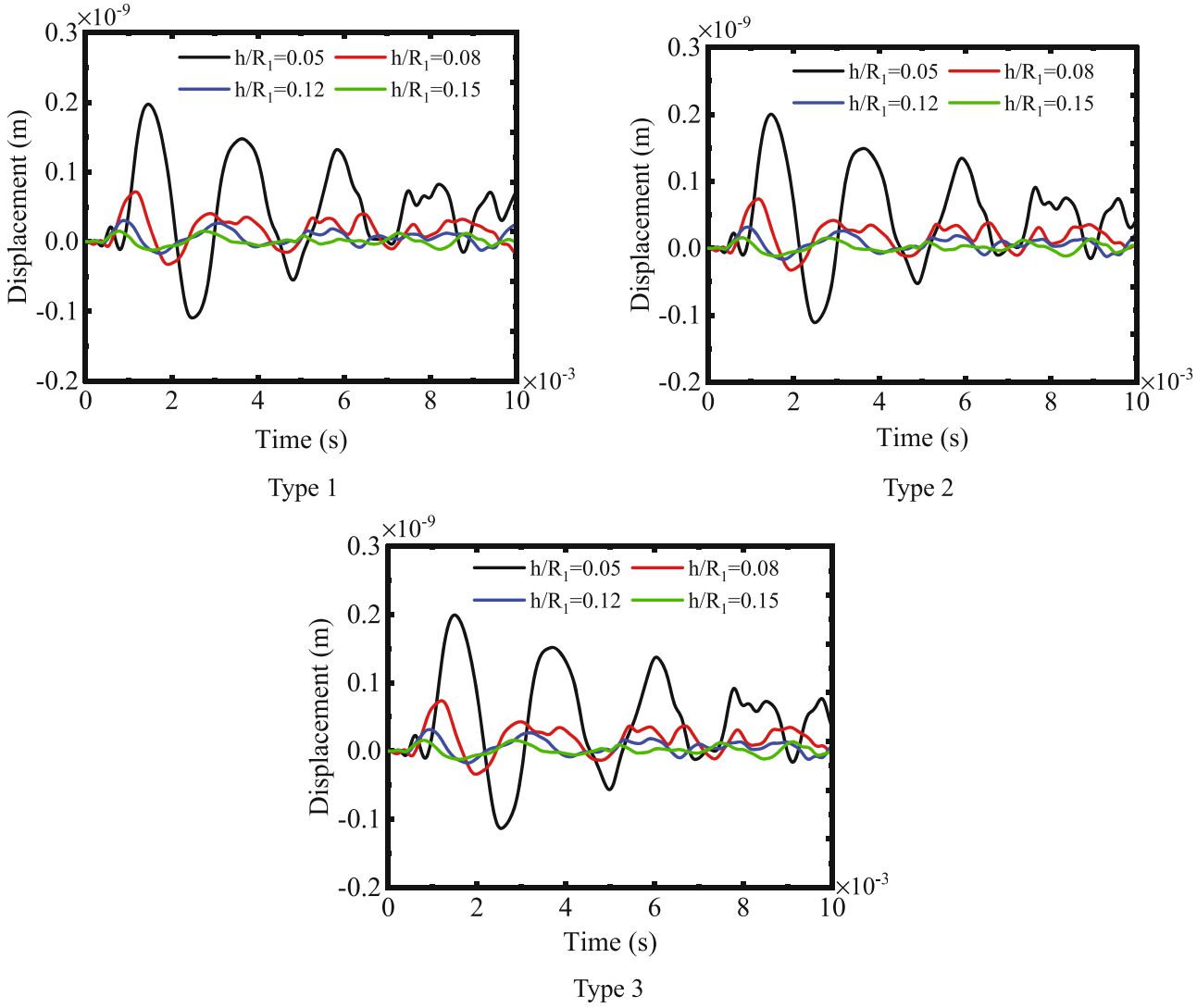

Figure 10: Effect of thickness ratio on transient response of FGP spherical shell (R = 2 m, φ_0 = 30°, φ_1 = 150°, e_0 = 0.2, load position: (π/2, 0), observation location: (2π/3, 0), $t = \tau$ = 10 ms, Δt = 0.01 ms, S–S boundary condition).

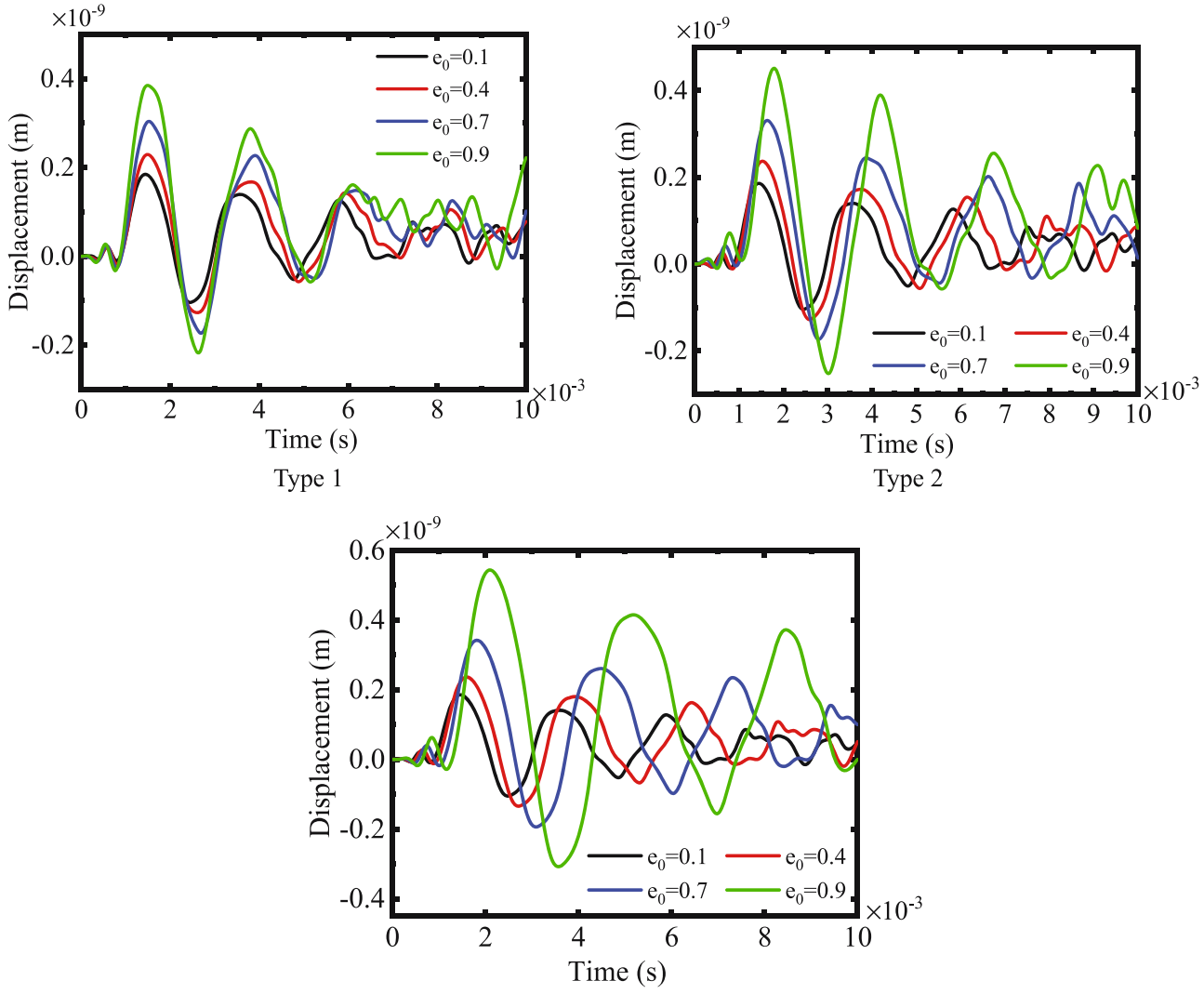

Figure 11: Effect of porosity ratios on transient response of FGP spherical shell (R = 2 m, h = 0.1 m, φ_0 = 30°, φ_1 = 150°, load position: (π/2, 0), observation location: (2π/3, 0), $t = \tau$ = 10 ms, Δt = 0.01 ms, S–S boundary condition).

the response curve is gradually moving to the right side. The reason may lie in that the increase in the thickness ratio causes the mass matrix of the FGP spherical shell to increase.

Figure 8 provides the effect of porosity coefficients on the steady-state response of the FGP spherical shell. It can be found that as the porosity coefficient increases, no matter the porosity distribution types, the peaks of the response curve are slightly moving to the left. This is because the stiffness falls with the increase of the porosity coefficient. Hence, lower porosity coefficients are selected in engineering applications.

3.2.2 Transient response

Figure 9 displays the comparison of both the proposed method and ABAQUS software on the transient response of the FGP spherical shell with the C–C boundary condition. The contrastive study illustrates that the proposed method has sufficient accuracy in predicting the transient response. After the verification, the parametric study can proceed.

Figure 10 investigates the effect of thickness ratio on the transient response of the FGP spherical shell. The load position of the pulse is (π/2, 0), and the observation location is (2π/3, 0). As can be seen in Figure 10, the thickness ratios have a remarkable effect on the peaks of the transient response. The peak of the transient response grows up with the increase of the thickness ratio, and this phenomenon becomes more obvious when the thickness ratio reaches 0.05. A possible explanation for this may be that the spherical shell with a higher thickness ratio performs better shock resistance.

Figure 11 explores the effect of porosity ratios on the transient response of the FGP spherical shell. It is worth

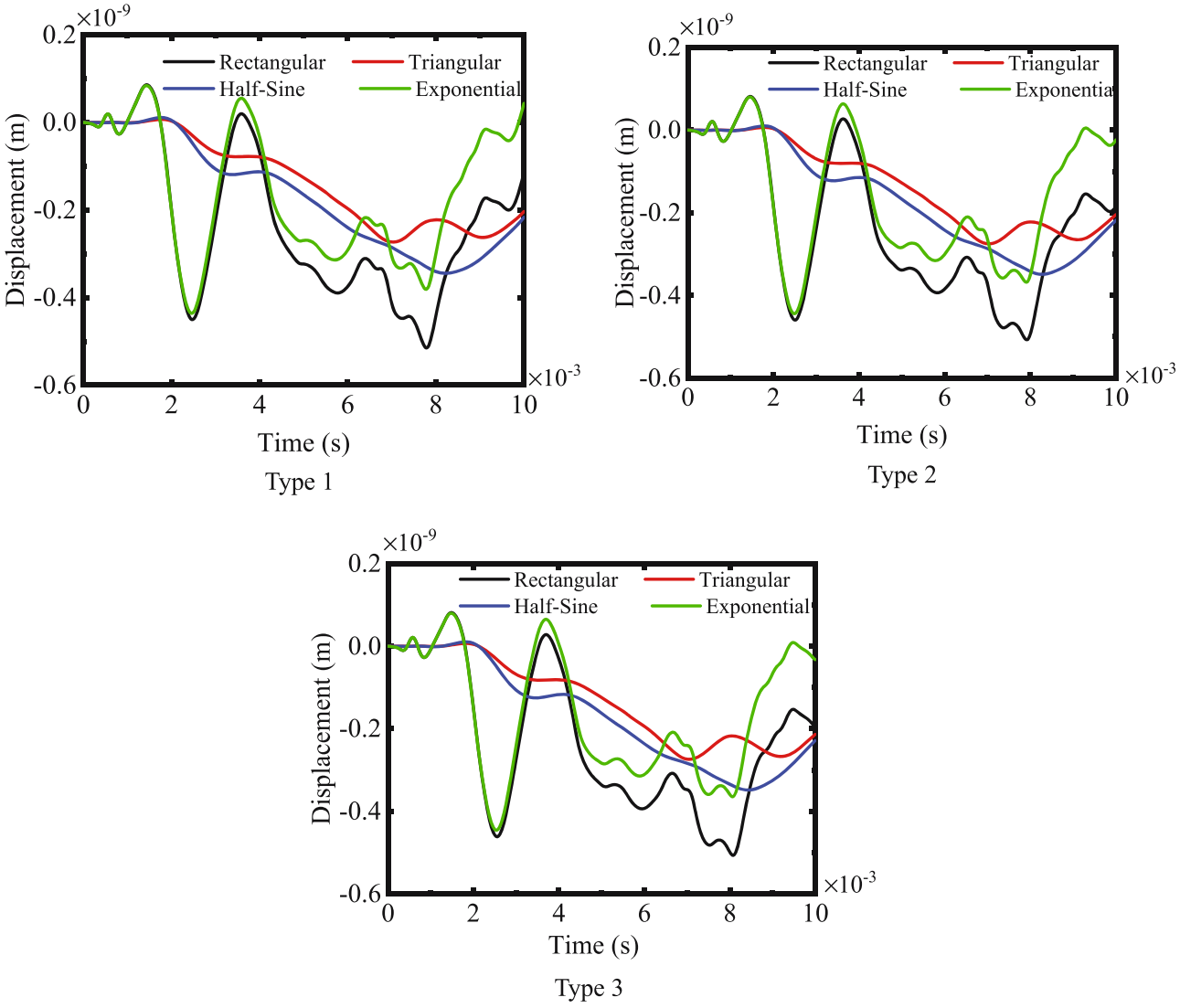

Figure 12: Effect of load types on transient response of FGP spherical shell (R = 2 m, h = 0.1 m, φ_0 = 30°, φ_1 = 150°, load position: (π/2, 0), observation location: (2π/3, 0), t = 10 ms, τ = 5 ms, Δt = 0.01 ms, E1–E2 boundary condition).

noting that the growth of the porosity coefficient cannot delay the arrival time of the shock wave peaks but can raise the amplitude of the shock wave peaks. This is because the porosity coefficient only affects the stiffness and has no connection with the pulse frequency. Hence, reducing the porosity ratios is an effective way to improve the stability performance of the FGP spherical shell under the random shock wave.

Figure 12 investigates the transient response of the FGP spherical shell with various load types. The triangular pulse can markedly delay the arrival time of the peaks of the loading pulse and decline the loading pulse peaks. This is because the shape and duration of the shock waves have a significant effect on the dynamic response of the FGP spherical shell. The spherical shell's transient response can be regulated by controlling the type of loading pulse so that the risk of damage to the structure, under external load, can be reduced.

4 Conclusion

In this study, the dynamic behaviors of the FGP spherical shell with elastic boundary conditions were investigated. Based on the aforementioned work, the findings of this study are summarized as follows:

1) The calculated results of the model proposed by the comparative study agree well with the available data, with a maximum error of less than 1%. The study

reveals that the intrinsic frequency increases rapidly along with the increase of the boundary stiffness and the decrease of the porosity. Besides, compared with the FEM, the proposed method has sufficient accuracy in predicting the transient response.

2) The boundary conditions significantly affect the steady-state response. Specifically, fluctuations at the E4–E4 boundary condition reach about 10% less than at the other boundary conditions. Also, increasing the thickness ratio increases the stiffness of the structure and leads to a decrease in the peak steady-state response. The dynamic performance of the structure can be improved by adjusting the constraint conditions.
3) As the thickness ratio increases, the peaks of the transient response gradually decrease, and a higher thickness ratio provides better impact resistance. However, an increase in porosity cannot delay the arrival time of the shock wave peak but increase the amplitude of the shock wave. To suppress the structure vibration, a large thickness ratio and lower porosity are suggested to be considered.

Although FGP is widely used due to its excellent stiffness-to-weight ratio, the structural stiffness weakened by internal pores always is an inevitable problem. Hence, looking for an optimal solution will be the key point in future work.

Funding information: This study was supported by the Natural Science Foundation of Shandong Province (Grant No. ZR2022QE086); Natural Science Foundation of Shandong Province under Grant ZR2023ME133.

Conflict of interest: The authors state no conflict of interest.

Ethical approval: This article does not contain any studies with human participants or animals performed by any of the authors.

Data availability statement: Some or all data, models, or code that support the findings of this study are available from the corresponding author upon reasonable request.

References

[1] Zhu H, Liu D, Bao H. Influence of initial imperfections on PMMA spherical shell. Adv Mater Sci Eng. 2022;2022. doi: 10.1155/2022/3481368.
[2] Subramani M, Ramamoorthy M, Arumugam AB. Free and forced vibration characteristics of CNT reinforced composite spherical sandwich shell panels with MR elastomer core. Int J Struct Stab Dyn. 2021;21:2150136.
[3] Kim K, Kumchol M, Kwak S. Free vibration analysis of laminated composite spherical shell with variable thickness and different boundary conditions. J Vib Eng & Technol. 2022;10:689–714.
[4] Sobhani E. Vibrational characteristics of fastening of a spherical shell with a coupled conical-conical shells strengthened with nanocomposite sandwiches contained agglomerated CNT face layers and GNP core under spring boundary conditions. Eng Anal Bound Elem. 2023;146:362–87.
[5] Adin H, Adin MS. Effect of particles on tensile and bending properties of jute epoxy composites. Mater Test. 2022;64:401–11.
[6] Song M, Ge S. Dynamic response of composite shell under axial explosion impact load in tunnel. Thin-Walled Struct. 2013;67:49–62.
[7] Adin MS, Kılıçkap E. Strength of double-reinforced adhesive joints. Mater Test. 2021;63:176–81.
[8] Hamit A, Sağlam Z, Adin MS. Numerical investigation of fatigue behavior of non-patched and patched aluminum/composite plates. Eur Mech Sci. 2021;5:168–76.
[9] Panda SK, Singh BN. Nonlinear free vibration of spherical shell panel using higher order shear deformation theory – A finite element approach. Int J Press Vessel Pip. 2009;86:373–83.
[10] Mahapatra TR, Panda SK. Nonlinear free vibration analysis of laminated composite spherical shell panel under elevated hygrothermal environment: A micromechanical approach. Aerosp Sci Technol. 2016;49:276–88.
[11] Ram KSS, Babu TS. Free vibration of composite spherical shell cap with and without a cutout. Comput Struct. 2002;80:1749–56.
[12] Su Z, Jin G, Shi S, Ye T. A unified accurate solution for vibration analysis of arbitrary functionally graded spherical shell segments with general end restraints. Compos Struct. 2014;111:271–84.
[13] Duc ND, Quang VD, Anh VTT. The nonlinear dynamic and vibration of the S-FGM shallow spherical shells resting on an elastic foundations including temperature effects. Int J Mech Sci. 2017;123:54–63.
[14] Xie K, Chen M, Li Z. A semi-analytical method for vibration analysis of thin spherical shells with elastic boundary conditions. J Vibroengineering. 2017;19:2312–30.
[15] Li Q, Wu D, Gao W. Static bending and free vibration of organic solar cell resting on Winkler-Pasternak elastic foundation through the modified strain gradient theory. Eur J Mech-A/Solids. 2019;78:103852.
[16] Li Z, Zheng J, Chen Y, Sun Q, Zhang Z. Effect of temperature variations on the stability mechanism of the confined functionally graded porous arch with nanocomposites reinforcement under mechanical loading. Compos Part B: Eng. 2019;176:107330.
[17] Li Z, Zheng J, Zhang Z. Mechanics of the confined functionally graded porous arch reinforced by graphene platelets. Eng Struct. 2019;201:109817.
[18] Li Z. Exploration of the encased nanocomposites functionally graded porous arches: Nonlinear analysis and stability behavior. Appl Math Model. 2020;82:1–16.
[19] Liu Z, Yang C, Gao W. Nonlinear behaviour and stability of functionally graded porous arches with graphene platelets reinforcements. Int J Eng Sci. 2019;137:37–56.
[20] Xue Y, Jin G, Ma X, Chen H, Ye T, Chen M. Free vibration analysis of porous plates with porosity distributions in the thickness and in-plane directions using isogeometric approach. Int J Mech Sci. 2019;152:346–62.

[21] Tran TT, Tran VK, Pham QH, Zenkour AM. Extended four-unknown higher-order shear deformation nonlocal theory for bending, buckling and free vibration of functionally graded porous nano-shell resting on elastic foundation. Compos Struct. 2021;264.
[22] Wu D, Liu A, Huang Y, Huang Y, Pi Y, Gao W. Dynamic analysis of functionally graded porous structures through finite element analysis. Eng Struct. 2018;165:287–301.
[23] Cünedioğlu Y, Beylergil B. Free vibration analysis of laminated composite beam under room and high temperatures. Struct Eng Mech. 2014;51:111–30.
[24] Cunedioglu Y, Beylergil B. Free vibration analysis of damaged composite beams. Struct Eng Mech: An Int J. 2015;55:79–92.
[25] Jahwari F, Naguib HE. Analysis and homogenization of functionally graded viscoelastic porous structures with a higher order plate theory and statistical based model of cellular distribution. Appl Math Model. 2016;40:2190–205.
[26] Guan X, Sok K, Wang A. A general vibration analysis of functionally graded porous structure elements of revolution with general elastic restraints. Compos Struct. 2019;209:277–99.
[27] Duc ND, Seung-Eock K, Khoa ND, Chan DQ. Nonlinear buckling and post-buckling analysis of shear deformable stiffened truncated conical sandwich shells with functionally graded face sheets and a functionally graded porous core. J. Sandw. Struct. Mater. 2021;23(7):2700–35.
[28] Van TN, Khoa ND, Duc ND. Nonlinear dynamic analysis of piezoelectric functionally graded porous truncated conical panel in thermal environments. Thin-Walled Struct. 2020;154:106837.
[29] Duc ND, Seung-Eock K, Khoa ND. Nonlinear buckling and post-buckling analysis of shear deformable stiffened truncated conical sandwich shells with functionally graded face sheets and a functionally graded porous core. J Sandw Struct Mater. 2021;23:2700–35.
[30] Zhao J, Wang Q, Deng X, Choe K, Xie F, Shuai C. A modified series solution for free vibration analyses of moderately thick functionally graded porous (FGP) deep curved and straight beams. Compos Part B: Eng. 2019;165:155–66.
[31] Guan X, Sok K, Wang A, Shuai C, Tang J, Wang Q. A general vibration analysis of functionally graded porous structure elements of revolution with general elastic restraints. Compos Struct. 2019;209:277–99.
[32] Salehipour H, Shahsavar A, Civalek O. Free vibration and static deflection analysis of functionally graded and porous micro/nanoshells with clamped and simply supported edges. Compos Struct. 2019;221:110842.
[33] Gao ZJ, Li H, Zhao J, Guan JL, Wang QS. Analyses of dynamic characteristics of functionally graded porous (FGP) sandwich plates with viscoelastic materials-filled square-celled core. Eng Struct. 2021;248:113242.
[34] Qin B, Zhong R, Wang Q, Zhao X. A Jacobi-Ritz approach for FGP beams with arbitrary boundary conditions based on a higher-order shear deformation theory. Compos Struct. 2020;247:112435.
[35] Li HC, Pang FZ, Chen HL, Du Y. Vibration analysis of functionally graded porous cylindrical shell with arbitrary boundary restraints by using a semi analytical method. Compos Part B-Eng. 2019;164:249–64.
[36] Karami B, Janghorban M, Tounsi A. Galerkin's approach for buckling analysis of functionally graded anisotropic nanoplates/different boundary conditions. Eng Comput. 2019;35:1297–316.
[37] Li H, Pang F, Ren Y, Miao X, Ye K. Free vibration characteristics of functionally graded porous spherical shell with general boundary conditions by using first-order shear deformation theory. Thin-Walled Struct. 2019;144:106331.